JGR Solid Earth

RESEARCH ARTICLE
10.1029/2021JB023656

Crustal and Uppermost Mantle Heterogeneities Across the Ailaoshan Red River Shear Zone, SE Tibet: Implications for Cenozoic Magmatic Activity

Mijian Xu[1,2,3], Dayong Yu[1], Zhouchuan Huang[1], Ping Tong[2,3,4], Shijie Hao[2,3], Youyi Ruan[1], and Cunrui Han[1,5]

[1]School of Earth Sciences and Engineering, Nanjing University, Nanjing, China, [2]Division of Mathematical Sciences, School of Physical and Mathematical Sciences, Nanyang Technological University, Singapore, Singapore, [3]Earth Observatory of Singapore, Nanyang Technological University, Singapore, Singapore, [4]Asian School of the Environment, Nanyang Technological University, Singapore, Singapore, [5]Department of Earth and Planetary Sciences, Birkbeck, University of London, London, UK

Key Points:

- Receiver function analysis reveals detailed crustal and uppermost mantle structures beneath the Ailaoshan Red River shear zone (ARSZ)
- Significant low-velocity zones are imaged both in the mid-lower crust and asthenosphere
- Magmatic activity in the ARSZ is inferred to originate from the asthenosphere

Supporting Information:

Supporting Information may be found in the online version of this article.

Correspondence to:

M. Xu and D. Yu,
gomijianxu@gmail.com;
yudy@nju.edu.cn

Citation:

Xu, M., Yu, D., Huang, Z., Tong, P., Hao, S., Ruan, Y., & Han, C. (2022). Crustal and uppermost mantle heterogeneities across the Ailaoshan Red River shear zone, SE Tibet: Implications for Cenozoic magmatic activity. *Journal of Geophysical Research: Solid Earth*, *127*, e2021JB023656. https://doi.org/10.1029/2021JB023656

Received 17 NOV 2021
Accepted 27 MAY 2022

Author Contributions:

Conceptualization: Mijian Xu
Data curation: Dayong Yu
Formal analysis: Mijian Xu, Youyi Ruan, Cunrui Han
Funding acquisition: Dayong Yu, Zhouchuan Huang, Ping Tong
Methodology: Mijian Xu, Ping Tong, Youyi Ruan
Project Administration: Dayong Yu
Resources: Dayong Yu
Software: Mijian Xu, Ping Tong, Youyi Ruan
Supervision: Dayong Yu, Zhouchuan Huang, Ping Tong
Validation: Mijian Xu
Visualization: Mijian Xu
Writing – original draft: Mijian Xu

Abstract The Ailaoshan Red River shear zone (ARSZ) was formed in the Mesozoic as a suture zone between the Indochina block and the Yangtze craton. Since the Cenozoic, block extrusion due to the Indo-Asian collision has reactivated the fault zone and caused large-scale shearing. Affected by the Cenozoic orogeny, a large volume of magmatic and metamorphic rocks developed in the ARSZ, forming many orogenic gold deposits. However, the source and the geodynamic process of these magmatic activities are still unclear. To gain a basic understanding of the subsurface magmatic activity, we deployed a dense array of 24 broadband seismic stations across the Daping and Chang'an gold deposits at the southern end of the ARSZ. Receiver function analysis, common conversion point stacking, and a joint inversion of receiver functions and surface wave dispersions are performed to image the detailed structure of the crust and uppermost mantle. Low-velocity zones in the mid-lower crust and thinned lithosphere (~70 km) are imaged under the ARSZ. The observed subsurface structures are verified by 3D numerical modeling with the SEM-FK method. We speculate that the mantle upwelling caused by lithospheric delamination has provided the main source of the mantle component in the magmatic rocks since ~35 Ma; afterward, high temperatures produced partial melting in the lower crust, which was emplaced along active shear zones.

Plain Language Summary The Cenozoic Indo-Asian collision caused a large amount of magmatic activity in the Ailaoshan Red River shear zone (ARSZ), accompanied by orogenic gold deposits and geothermal resources. The crustal and uppermost mantle structures are imaged with seismic methods for understanding the process of magmatic activity. Compared with synthetic teleseismic waveforms with a 3D numerical simulation under cartesian coordinate, we find low-velocity zones in the mid-lower crust and uppermost mantle, as well as the thinning lithosphere under the ARSZ and the Indochina block. Based on our observations and previous geochemical studies, we speculate that the delamination of the lithosphere causes the hot upper mantle material to upwell along the shear zone, leading to significant magmatic activity.

1. Introduction

The Ailaoshan Red River shear zone (ARSZ), bounded by the Ailaoshan fault (ALSF) and the Red River fault (RRF), is a suture between the Indochina block and the Yangtze craton formed from the Permian to the Triassic (Figures 1a and 1b; Lai et al., 2014; Metcalfe, 1996, 2002; X. Wang et al., 2000). In the Cenozoic (ca. 35-17 Ma), the Indo-Asian continental collision and the induced lateral extrusion of the Indochina block resulted in large-scale shearing along the reactivated ARSZ (Tapponnier et al., 1990, 2001). During the same period, significant magmatic activity caused by shearing and orogeny occurred, which was confirmed by granites and granitic metamorphic rocks in the shear zone (J. Liu et al., 2020; Searle et al., 2010; X. Chen et al., 2015). Isotopic dating and synthesis of structural data of the rocks indicate that the magmatic activity in the ARSZ has two phases: one is from ca. 41 to 30 Ma with crustal and upper mantle sources, and the other is from ca. 28 to 20 Ma with only crustal sources (J. Liu et al., 2020).

Accompanying the coeval shearing and magmatic activity (ca. 36–29 Ma), many porphyries and orogenic gold deposits are found in the southern ARSZ, such as the Daping and Chang'an gold deposits (J. Zhang et al., 2014;

Writing – review & editing: Dayong Yu, Zhouchuan Huang, Ping Tong, Youyi Ruan, Cunrui Han

Sun et al., 2009; Y. Chen et al., 2014). Synthetic isotope geochemical analysis suggests that the deposits were derived from asthenospheric upwelling and crustal partial melting (Y. Chen et al., 2014). However, it is still doubtful whether there are molten bodies corresponding to these magmatic activities and ore-forming fluids in the crust or upper mantle.

Geophysical studies have found evidence for crustal and upper mantle heterogeneities along and around the ARSZ. For instance, receiver function studies suggest that the lithospheric thickness is ~70–80 km, much thinner than the global average (D. Yu & Wang, 2018; Pasyanos et al., 2014; Yang et al., 2017). Seismic tomography revealed low-velocity zones in the upper mantle under the Indochina block (Fu et al., 2017; Huang et al., 2015, 2019; Lü et al., 2014; Z. Zhang et al., 2020), interpreted as hot materials induced by mantle upwelling or lithospheric delamination.

The heat flows near the ARSZ are 60–90 mW/m^2, significantly higher than those in the craton (less than 50 mW/m^2) (e.g., Tao & Shen, 2008). There are also a large number of hot springs near the ARSZ (Shi & Wang, 2017). These studies indicate strong thermal activity in the crust in our study region. Low crustal velocity and resistivity zones are found near the ARSZ (e.g., Bao, Sun, et al., 2015; N. Yu et al., 2020), indicating weak materials in the crust. Recent studies using seismic data from short-period nodes have revealed detailed crustal features. Ambient noise tomography shows a high-velocity zone in the upper crust (6–10 km), which is related to the Ailaoshan metallogenic belt (Zheng et al., 2021). A High-frequency receiver function study has provided accurate crustal thicknesses and average crustal V_P/V_S ratios via $H-\kappa$ stacking (L. Zhang et al., 2020). The V_P/V_S ratios in the ARSZ are notably larger than those in the Indochina block and Yangtze craton, indicating that the Cenozoic magmatic activity resulted in weak lower crust in the ARSZ (L. Zhang et al., 2020). However, limited by data resolution and/or techniques in previous studies, there are still unresolved problems: What are the geometric features of the weak materials under the ARSZ? Are these weak materials directly related to the magmatic activity inferred from the geochemical analysis?

To answer these questions, we use the P-wave receiver functions (PRFs) technique to image the crustal and upper mantle structure across the ARSZ with the data recorded by a newly deployed dense seismic array. The common conversion point (CCP) stacking method is used to highlight subsurface discontinuities, such as the Moho, intracrustal discontinuities and the potential lithosphere-asthenosphere boundary (LAB). The joint inversion of Rayleigh wave dispersions and PRFs is conducted to reveal S-wave velocity structures. Thus, we obtain the detailed crustal and uppermost mantle structures beneath the ARSZ and its surrounding areas.

2. Data and Method

2.1. Data

From November 2017 to January 2020, we deployed a linear array of 24 broadband seismic stations (black triangles in Figure 1b) with an average spacing of ~10 km across the Indochina block, ARSZ, and Yangtze craton. Each seismograph was equipped with a Reftek-130/130s data logger and a Guralp CMG-40T/3T sensor. Two temporary stations deployed by ChinArray I (red triangles Figure 1b) from October 2011 to March 2014 are selected to fill two relatively large gaps between the stations. Seismograms of 542 teleseismic events with epicentral distances from 30° to 90° and magnitudes ≥ Mw 5.5 (bottom right inset in Figure 1) recorded at those 26 seismic stations are selected and preprocessed for further analysis.

2.2. Receiver Functions

Following M. Xu et al. (2020), we first remove the mean shift and linear trend of seismic waveforms. Then, we apply a bandpass filter of 0.05–2 Hz on the waveforms and trim them from 10 s before to 120 s after the theoretical P arrival. By setting the Gaussian factor to be 2 in the deconvolution, the PRFs are calculated with the time-domain iterative deconvolution method (Ligorría & Ammon, 1999). Finally, a total of 2385 PRFs remained after manual quality control.

To visually check the quality of the PRFs, we stack and sort them by ray parameter. The P_ms, PpPs and PsPs + PpSs phases are visible around their predicted delay times (P_ms at 4–5 s, PpPs at 14–16 s; PsPs + PpSs at 18–20 s) (Figure 2). On the one hand, disordered negative phases are visible at 6–9 s, and the time delays are close to those of the converted phases at 60–70 km, coinciding with the depth of the LAB in the study region (Pasyanos

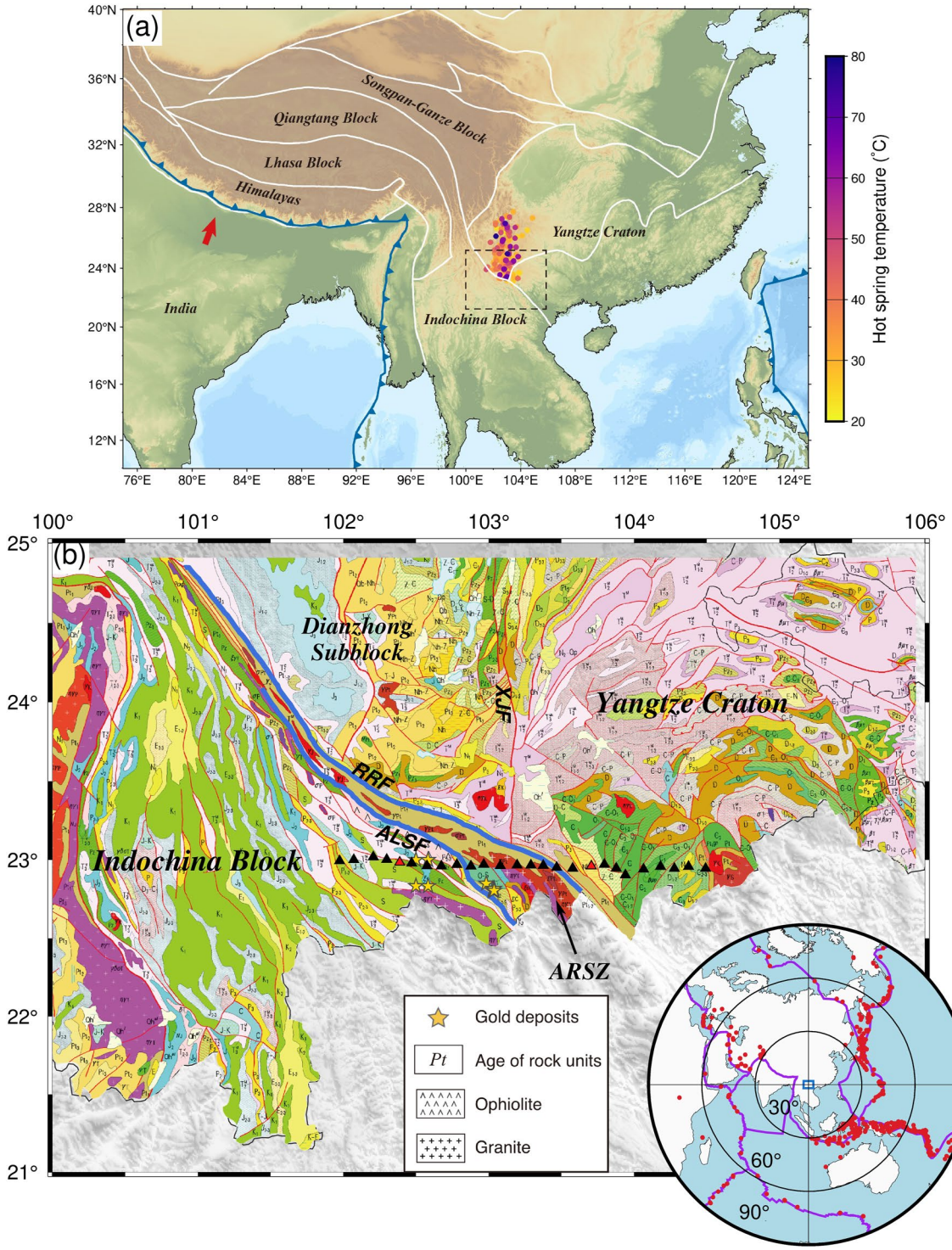

Figure 1. (a) Tectonic background of east Asia. The blue lines with triangles denote plate boundaries. The white lines denote sutures. Colored dots denote the temperature of hot springs in SE Tibet (Shi & Wang, 2017). The black dashed box denotes the study region. (b) Geological map of the Ailaoshan Red River shear zone (ARSZ) and adjacent regions (China Geology Survey, 2002). The black and red triangles denote seismic stations. The red lines represent faults. The blue lines represent the Ailaoshao Fault (ALSF) and Red River Fault (RRF). The abbreviations are XJF: Xiaojiang fault, ARSZ: Ailaoshan-Red-River shear zone. (Bottom-right inset) The red circles show the earthquakes used in this study. The purple curves represent the plate boundaries.

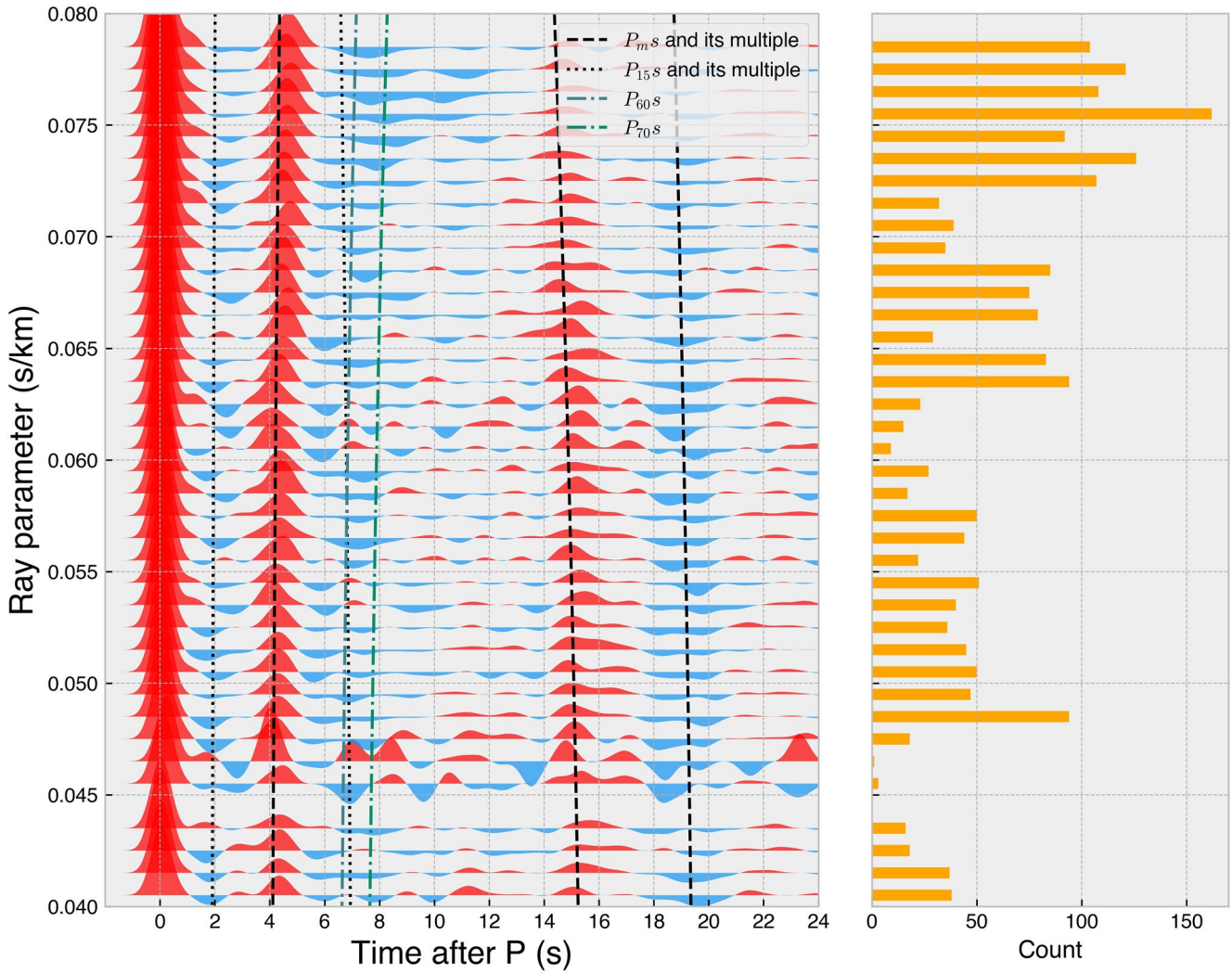

Figure 2. Binned stacked P-wave receiver functions (PRFs) arranged by ray parameters. Red and blue colors denote positive and negative peaks, respectively. Black dashed lines show the theoretical time difference of the P_ms phase and its multiples. Black dotted lines show the theoretical time difference of the P_{15}s phase and its multiples. Blue and green dot-and-dash lines represent the theoretical time difference of the P_{60}s and P_{70}s, respectively.

et al., 2014). On the other hand, negative crustal phases at ~2 s are clear before the P_ms phases, while the corresponding multiple phases appear at ~7 s, which is close to the time delay of the converted phases at depths of 60–70 km. Therefore, the negative phase at 6–9 s may be multiples of crustal phases or may be generated by the LAB or both; further discussion is in Section 4.

2.3. Common Conversion Point Stacking

CCP stacking is used to reveal the lateral variations of the Moho and other velocity interfaces. First, we calculate the locations of the PRFs pierce points in the 1D AK135 model (Kennett et al., 1995) at 1-km depth intervals. Second, we convert the PRFs from the time domain to the depth domain in 1D and 3D velocity models. The 1D velocity models include the AK135 model and the 1D model from the joint inversion of PRFs and surface wave dispersions at each station. For the 3D velocity model, Vp and Versus are interpolated from a regional velocity model (Z. Zhang et al., 2020) according to the locations of pierce points determined in the 1D AK135 model. Because of the large variation in elevation along the profile, we apply station elevation corrections such that PRFs in the depth domain are in respect to sea level. Finally, we stack the depth-domain PRFs along the linear array whose pierce points fall in the rectangular bins (5 km interval), where the width was determined by the first Fresnel zone (M. Xu et al., 2020).

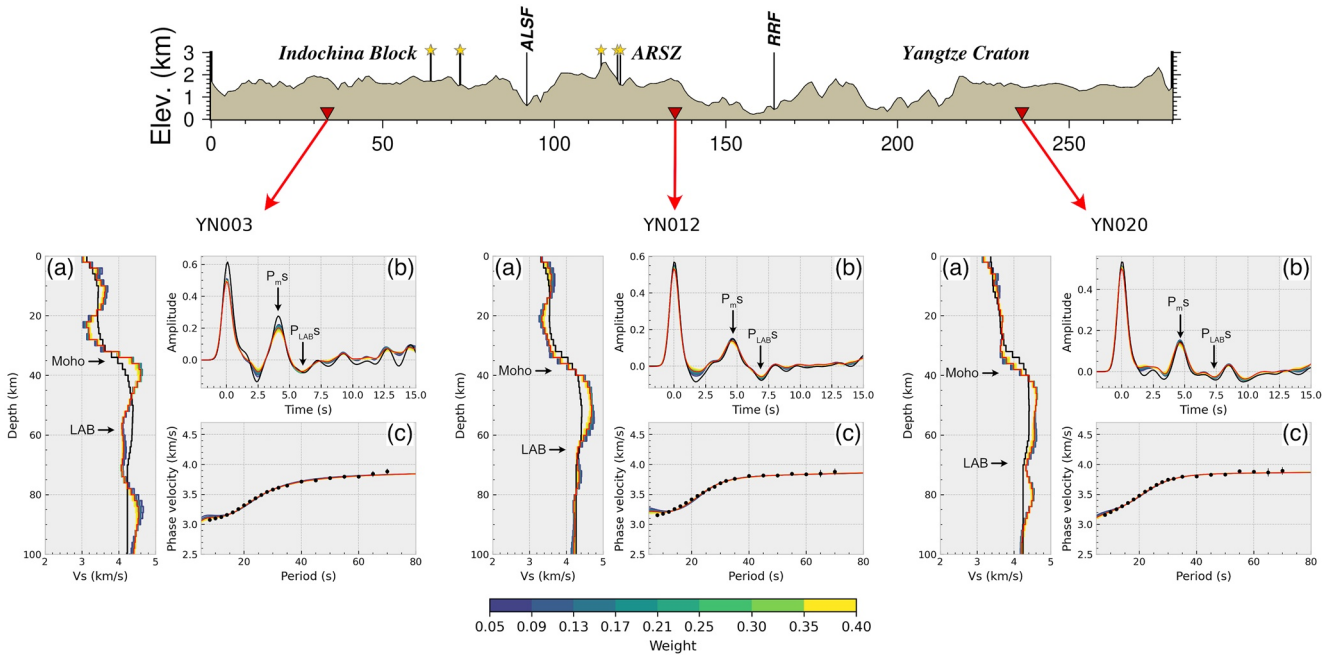

Figure 3. Examples of the joint inversion for stations YN003, YN012, and YN020. The locations of these stations are shown on the top elevation map. (a) The velocity model of the joint inversion. Colored lines denote inverted velocity models with different weights between surface wave dispersions and P-wave receiver functions (PRFs). The red line denotes the average velocity model. The black line denotes the initial model (Y. Liu et al., 2021). (b) Colored lines denote predicted PRFs derived from inverted velocity models with different weights. The red line denotes predicted PRFs from the average velocity model. The black line denotes observed PRFs. (c) Colored lines denote the predicted phase velocity dispersion from inverted velocity models with different weights. The red line denotes the predicted phase velocity dispersion from the average velocity model. Black dots represent the observed phase velocity dispersion (Shen et al., 2016).

2.4. Joint Inversion of PRFs and Surface Wave Dispersions

The joint inversion of PRFs and surface wave dispersion is an effective way to image the isotropic S-wave velocity structure in the crust and uppermost mantle (e.g., Bao, Sun, et al., 2015; Julià et al., 2000). The initial model of the inversion influences the final inverted velocity model (Li et al., 2017). A suitable initial model helps to obtain results close to the real model. SWChinaCVM-1.0 is a new community 3D velocity model of the crust and upper mantle in SE Tibet (Y. Liu et al., 2021). This model provides both P- and S-wave velocities from the joint inversion of body wave traveltimes, Rayleigh wave dispersions and ZH ratios. To construct 1D initial models, P- and S-wave velocities sampled at every 2 km beneath each station are directly extracted from the 3D velocity model. At each iteration of our inversion, P-wave velocities is directly computed from Versus by using the V_P/V_S value of the starting model.

To strengthen the amplitude of the conversion phases, we linearly stack the PRFs at each station after the move-out correction with a reference ray parameter of 0.065 s/km. However, some multiple phases are distorted after the move-out correction, and consequently, the stacking procedure reduces the amplitude of some multiple phases. Therefore, in the joint inversion we only use the PRFs in a time window that is from 5 s before to 15 s after the direct P arrival. Due to the interference of multiples, the inversion for deeper upper mantle structure involves more uncertainties, and hence we set the effective inversion depth from 0 to 100 km.

In the joint inversion, the Rayleigh wave phase velocity dispersions from 8–70 s are extracted from a phase velocity model for mainland China (Shen et al., 2016), which is derived from ambient noise surface wave tomography. Shen et al. (2016) used ambient noise data both from dense Chinarray and permanent stations in mainland China, leading to a 0.5° × 0.5° grid resolution. Because the resolution of surface wave dispersion data is lower than our station spacing, a reasonable weight between the surface wave dispersions and PRFs in the misfit function is conducive to improving reliabilities of the inversion. Thus, we do joint inversion with a series of weights from 0.60 to 0.95 with respect to PRFs. After 30 iterations, the stable S-wave velocities can be inverted with different weights (Figure 3). Both the Moho phases and the potential LAB phases in the predicted PRFs fit the observed

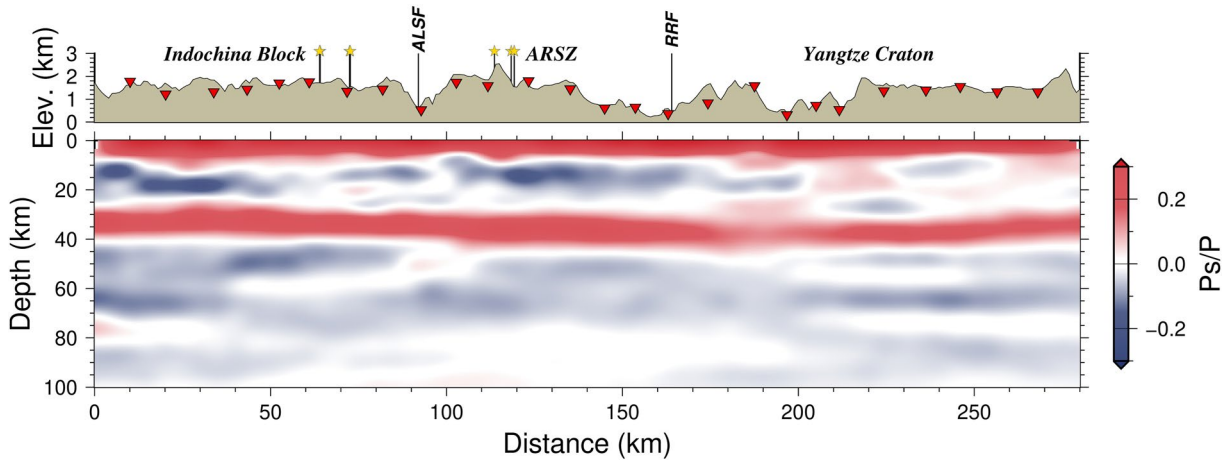

Figure 4. The common conversion point (CCP) stacking image along with the profile. The red colors indicate the positive phases; the blue colors indicate the negative phases. The topography along the profile is shown at the top. The yellow stars represent the gold deposits.

PRFs. In this study, we derived the final model by averaging the S-wave velocity models inverted with different weights. To further evaluate the influence of uncertainties in the phase velocity on the joint inversion, we randomly generate 400 phase velocity dispersions with ±5% anomalies applied on the phase velocities for the joint inversion. The inverted S-wave velocities is stable with a small standard deviation of less than 0.1 km/s in the crust and less than 0.18 km/s in the upper mantle (Figures S1 and S2 in Supporting Information S2). In addition, because the amplitude of the PRFs is not sensitive to the variation in S-wave velocities, when a negative seismic phase exists in the crust, the predicted receiver function has a large difference in amplitude on crustal negative phases, but the inverted S-wave velocities still show a small error at the corresponding depth.

3. Results

We used the 1D AK135 velocity model, the regional 3D velocity model developed by Z. Zhang et al. (2020) and the velocity model obtained via the joint inversion to correct the Ps—P time difference for PRFs and then performed CCP stacking in the three velocity models. All the CCP stacking images show very consistent Moho topographies, intracrustal phases and the potential LAB (Figures S3 and S4 in Supporting Information S1 and Figure 4). As follows, we discuss the main features of the CCP stacking image constructed in the velocity model obtained via the joint inversion (Figure 4 and Dataset S1). Consistent with the Moho depths from the S-wave velocity structures (Figure 5), the Moho depths are ∼34 and ∼36 km in Indochina and the ARSZ, respectively. In the Yangtze craton, the Moho depths gradually become shallower from ∼36 to ∼32 km. It is worth noting that the $P_m s$ phases are widened at locations that are ∼30 km east of the RRF (distance = ∼190 km), which probably results from the deep strike-slip of the RRF dips northeast (Schoenbohm et al., 2006). Thus, we infer that the fault has cut through the crust east of the RRF and may have destroyed the layered crustal structure, leading to a gentle crust-mantle transition. Negative phases are visible in the uppermost mantle, indicating the potential LAB. However, because of sediments and LVZs in the crust, multiples of crustal phases may interfere with upper mantle phases. We quantitatively discuss the interference in Section 4.2.

The weak zones usually have low-velocity anomalies. Figure 3 shows the fitness of the joint inversion and the 1D S-wave velocity beneath the three stations in different tectonic units. There are visible low-velocity zones in the mid-lower crust under the ARSZ and the Indochina block (YN003 and YN012) revealed by crustal negative phases of the PRFs (Figures 3a and 3b). Our S-wave velocity structures (Figure 5 and Dataset S2) and the CCP stacking profile (Figure 4) also show low-velocity zones and negative crustal phases in the mid-lower crust. The phases in CCP stacking correspond well to the gradient variation in Versus with depth (Figure S5 in Supporting Information S1). The S-wave velocities are less than 3.5 km/s in the mid-lower crust beneath the ARSZ and the Indochina block (Figure 5). In particular, a low-velocity zone (LVZ1) with an S-wave velocity less than 3.4 km/s is visible at depths of 15–25 km under the ARSZ (Figures 3b and 5), which is restricted by boundary faults (ALSF and RRF). Another crustal low-velocity zone is observed under the Indochina block with S-wave velocities from

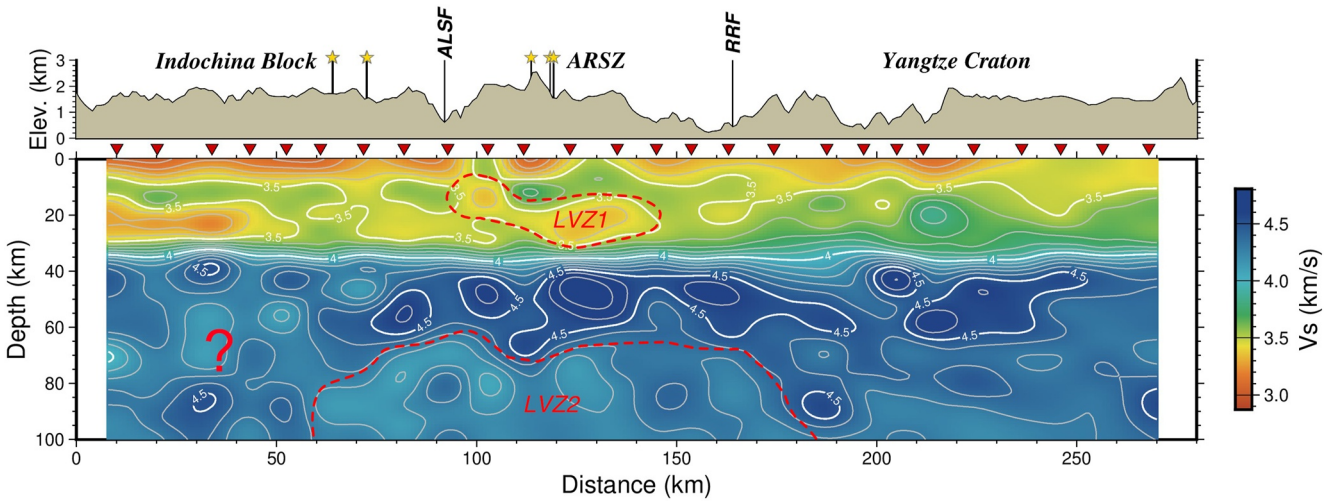

Figure 5. The inverted S-wave velocity structures along the profile. The dashed curves represent two major low-velocity zones (LVZ1 and LVZ2). The top inset has the same contents as those in Figure 3.

3.2 to 3.4 km/s (Figures 3a and 5). In contrast, under the Yangtze craton, only weak crustal phases are observed, and the S-wave velocity is almost larger than 3.5 km/s (Figures 3c and 5).

S-wave velocities below ~60 km depths are markedly smaller than those at 35–60 km depths (Figures 4 and 5). Despite being disturbed by crustal multiple phases, the CCP stacking profile shows continuous negative phases in the upper mantle. Sp receiver function studies (D. Yu & Wang, 2018; Yang et al., 2017) show that the lithospheric thickness is approximately 60–80 km in SE Tibet. Therefore, the low-velocity zone below ~60 km depth may represent the asthenosphere, and the negative phases in the upper mantle correspond to the LAB. However, the S-wave velocity under the Indochina block at 50–70 km depth is laterally heterogenic with that under the ARSZ (LVZ2) greater than 60 km. Together with the magmatic activity along the ARSZ with a depleted mantle component (Lai et al., 2014; Q. Wang et al., 2019), the low velocities in the uppermost mantle may indicate potential upwelling from the asthenosphere or even deeper mantle (e.g., Huang et al., 2015, 2019).

4. Numerical Verification of the Velocity Structure

4.1. Fitting With Observed PRFs

Numerical modeling of PRFs is widely used to examine the influence of crustal and mantle heterogeneities on seismic observations (e.g., Frederiksen & Bostock, 2000; L. Chen et al., 2005; L. Zhao et al., 2015). To confirm the main features in the crustal and uppermost mantle structure, we simulate the propagation of incident teleseismic P waves in the obtained velocity model and then compare the calculated waveforms with the observed PRFs. We use the 3D SEM-FK hybrid method to calculate the synthetic PRFs (Tong, Chen, et al., 2014; Tong, Komatitsch, et al., 2014). Figure 6a shows the structure of the computational spectral-element method (SEM) domain along the profile, which has a length of 380 km from 0 to 120 km depth. The SEM domain consists of three parts. The central area is embedded with the inverted 2D S-wave velocity model (Figure 6b). The length of the central area is 280 km along the X axis, while the depth is from 0 to 100 km along the Z axis. The Moho topography of the central area is extracted from the CCP stacking results (Figure 4). The P-wave velocity is calculated by using the empirical formula (Brocher, 2005) as:

$$V_P = 0.9409 + 2.0947V_S - 0.8206V_S^2 + 0.2683V_S^3 - 0.0251V_S^4. \quad (1)$$

Each of the two edge areas has a length of 50 km, and their model parameters are set the same as the 1D velocity model for the FK computation. The area in between the 2D and 1D velocity models is the buffer area, which bridges the inner 2D variation of the central area with the outer 1D variation of the FK computational domain via a linear transition. The buffer area is designed to ensure that the wavefield would not be scattered when propagating between the 2D and 1D models. We further extend the 2D model to a 3D model in the direction perpendicular

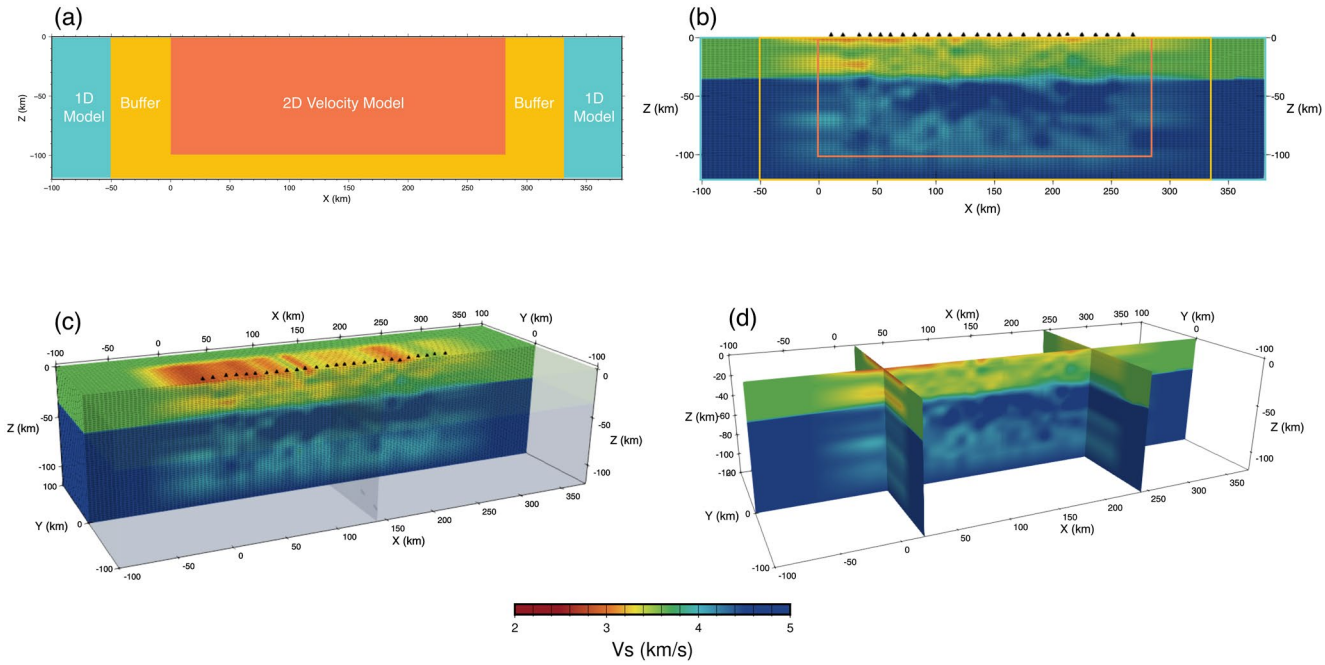

Figure 6. Diagrammatic sketch of the coupling of the 1D and 2D velocities in the SEM domain. (b) The spectral element mesh of the S-wave velocity along the XZ section. (c) The 3D view of the spectral element mesh. (d) Slices of S-wave velocity along the X- and Y-axis.

to the profile (the Y axis). On either side of the profile, the 3D velocity model has a 2D variation area with a width of 50 km, a buffer area with a width of 30 km, and a 20 km-wide 1D area (Figure 6d).

The stations are projected to the Cartesian coordinate system of the SEM domain along the profile (Figure 6c). We set up the injected plane waves as a series of virtual events with the back-azimuth from 0°–360° (with an interval of 30°) and ray-parameter from 0.04 to 0.08 s/km (increasing at every 0.004 s/km) (Figure 7a). With uneven distribution of back-azimuth and ray-parameter of observed PRFs, 63 virtual events are valid for forward simulation to fit with these observed PRFs. The incidence angles of the plane waves are determined by the ray parameters of the virtual events and computed with the Taup toolkit (Crotwell et al., 1999). The Gaussian factor of the source time function is $f_0 = 3.0$.

To evaluate the reliability of the inverted velocity model, we compare the synthetic PRFs with the observed PRFs. The 1D synthetic PRFs are derived by a 1D inverted model. The 3D synthetic PRFs are the stacked PRFs of all virtual events recorded by each station. We calculate the misfit in a time window from 1 to 8 s at each station:

$$\chi_m = \frac{1}{N}\sum_{i=1}^{N}\frac{(obs_i - pre_i)^2}{\sigma_m^2}, \tag{2}$$

where χ_m is the misfit of the mth station. obs_i and pre_i represent observed and synthetic PRFs at time t_i, respectively. N is the number of data points from 1 to 8 s σ_m is the root mean square of the observed PRF stacked with the mth station.

The observed PRFs are stacked after move-out corrections and are fitted with synthetic PRFs calculated with inverse models. The misfits of all stations calculated with Equation 2 (1D misfit) are less than 0.4 (Figure 7b). We also stack the synthetic PRFs calculated by the SEM-FK method with the same move-out corrections as applied to the observed PRFs. Figure 7b shows the fitness between the synthetic PRFs from the 3D velocity model and the observed PRFs. At most stations, the synthetic PRFs fit the $P_m s$ phase, the crustal phase, and the negative phase after the $P_m s$ phase well. We also calculate the misfit between the synthetic PRFs and the observed PRFs (3D misfit). The 3D misfits at most stations are less than 0.5, which is close to the 1D misfits. However, near the RRF, the 3D misfits (0.5–1.1) are much larger than the 1D misfits (0.1–0.3). We infer that because the profile does not

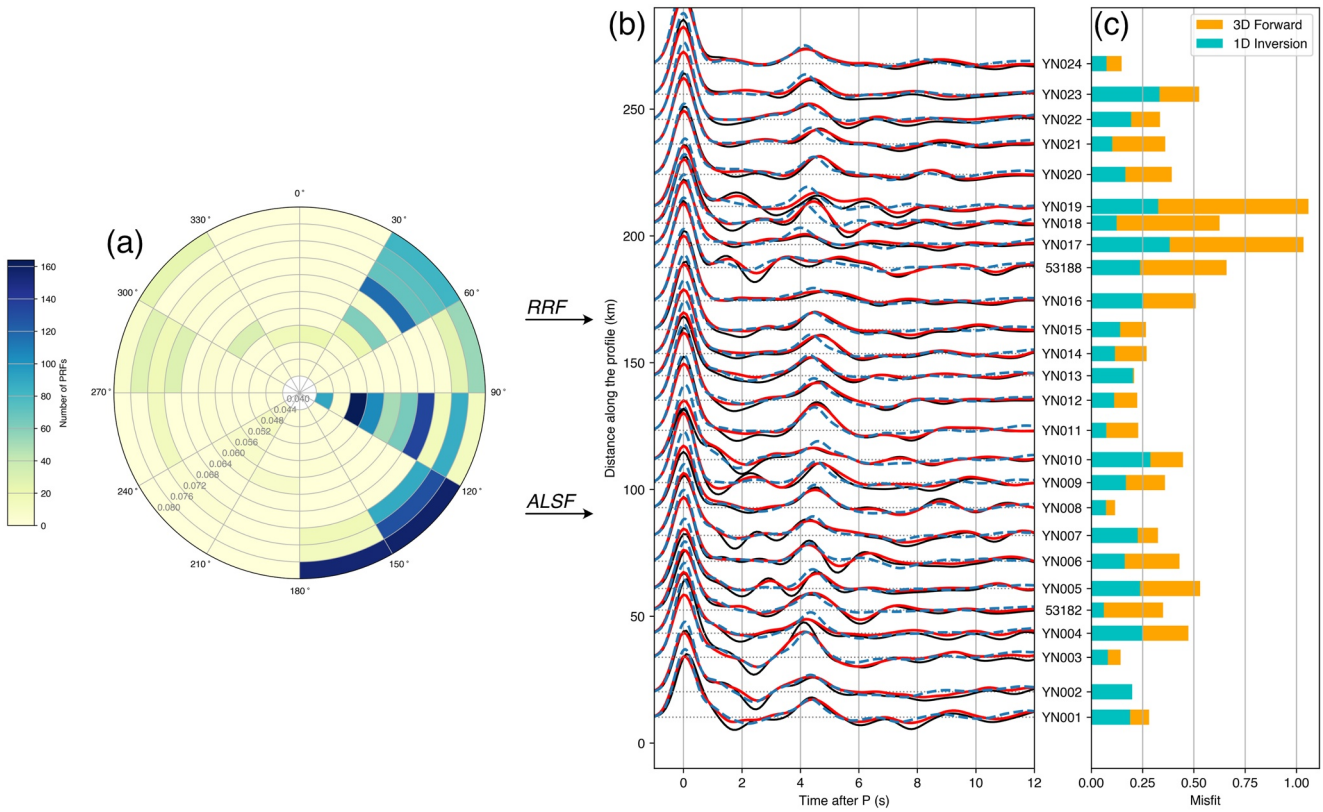

Figure 7. (a) 2D histogram of the number of P-wave receiver functions (PRFs) in different bins. The colors represent the number of observed receiver functions used for stacking in each bin. (b) The fitness between the stacked synthetic PRFs with the 3D velocity model (blue dashed lines), synthetic PRFs with the 1D velocity model (red lines), and the observed PRFs (black lines). (c) Misfits between synthetic and observed PRFs. Cyan bars denote 1D misfits. Yellow bars denote 3D misfits.

cross the RRF perpendicularly, resulting in differences in the velocity structure on both sides of the profile. The 1D joint inversion cannot eliminate these differences, resulting in some uncertainties near the RRF.

4.2. Comparison of CCP Stacking

Figure 8b shows the CCP stacking of synthetic PRFs computed in a 3D velocity model (Model I in Figure 8a). Compared with the observed CCP stacking, the synthetic data can recover the main features of the Moho well, such as the slightly deepening Moho in the ARSZ and the widening P_ms phases east of the RRF. Consistent with the observed CCP stacking (Figure 4), the 3D velocity model with the low-velocity zones in the crust produces the corresponding crustal negative phases under both the ARSZ and the Indochina block, therefore confirming the low-velocity zones there (Figure 8a).

Previous studies have found that the thickness of the lithosphere beneath SE Tibet is ~70–80 km (D. Yu & Wang, 2018; Hu et al., 2012; Pasyanos et al., 2014), which is much shallower than that beneath central Tibet (~100–150 km) (J. Zhao et al., 2010; Q. Xu, Bi, et al., 2019). Similarly, our CCP stacking profile reveals significant negative phases in the upper mantle (~60–70 km) (Figure 4), which may be produced by the LAB. However, multiple reverberations of crustal phases may interfere with the LAB phases. To better estimate the LAB phases, we set a new model (Model II) based on Model I, with a constant velocity in the upper mantle (Figure 8c). The CCP stacking of the synthetic PRFs in Model II shows two sets of negative phases in the upper mantle (Figure 8d). One is located at a depth of ~55 km spanning from 100 to 170 km along the X-axis (under the ARSZ). We have investigated the relationships between the Ps conversion phase and its multiple phases in the IASP91 model. When the converted phase appears at 15 km depth, its 3p1s (PpPs) will appear at 56 km depth (Figure 9), consistent with the negative phases in the upper mantle under the ARSZ (Figures 8b and 8d). This phase is the PpPs of the crustal negative phase. We mark this phase in Figure 8b and find that the multiple phases do not interfere with the LAB phase. Another set of negative phases is located at depths of 50–72 km from 0 to

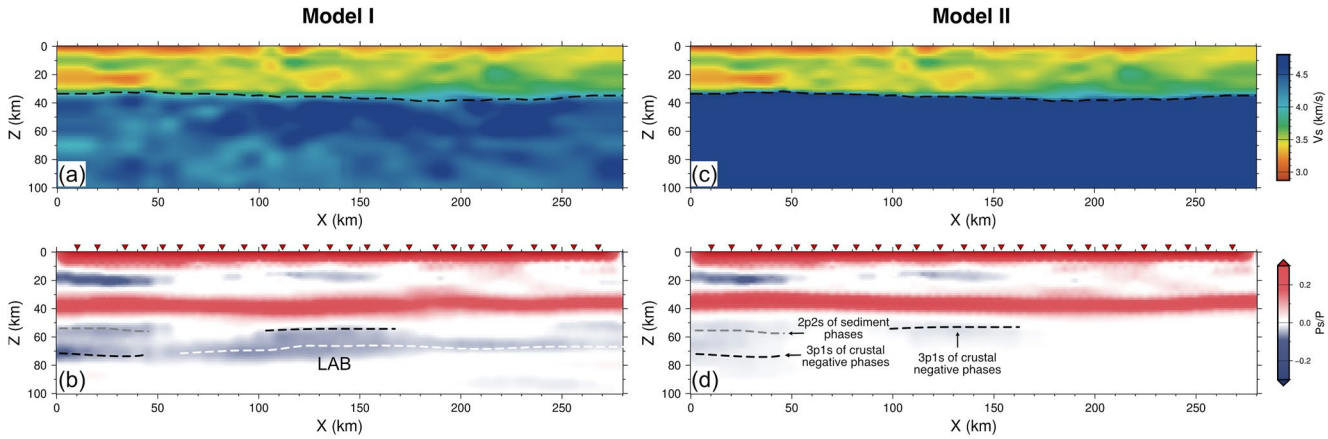

Figure 8. (a and c) The S-wave velocity of input Models I and II, respectively. Black dashed lines represent the Moho derived by common conversion point (CCP) stacking. (b and d) The synthetic CCP stacking profiles of Models I and II, respectively. The white dashed line represents the potential lithosphere-asthenosphere boundary (LAB). Black dashed lines represent the 3p1s of crustal phases. The gray dashed line represents the 2p2s of the sedimentary phase.

50 km along the X-axis (under the Indochina block). There are sedimentary positive phases (~10 km) and crustal negative phases (~20 km) in this area (Figures 8b and 8d). The 2p2s multiples (PsPs + PpSs) of the sedimentary phase appear at ~47 km depth (Figure 9), close to the depth of the weakly negative phases in the uppermost mantle. The 3p1s multiples of the crustal negative phases appear at ~70 km depth, indicating a negative phase at 70 km depth. These phases interfere with the upper mantle structure under the Indochina block. Therefore, the LAB under the Indochina block is rarely revealed by CCP stacking. However, considering the low phase velocity and strong negative Ps phases in the mantle, the low-velocity zone under the Indochina block cannot be ignored. Compared with the CCP stacking image in Model I, Model II does not generate continuous negative phases in the upper mantle (Figure 8d). Thus, we confirm that along the profile, the LAB under the ARSZ and Yangtze craton is at ~70 km depth.

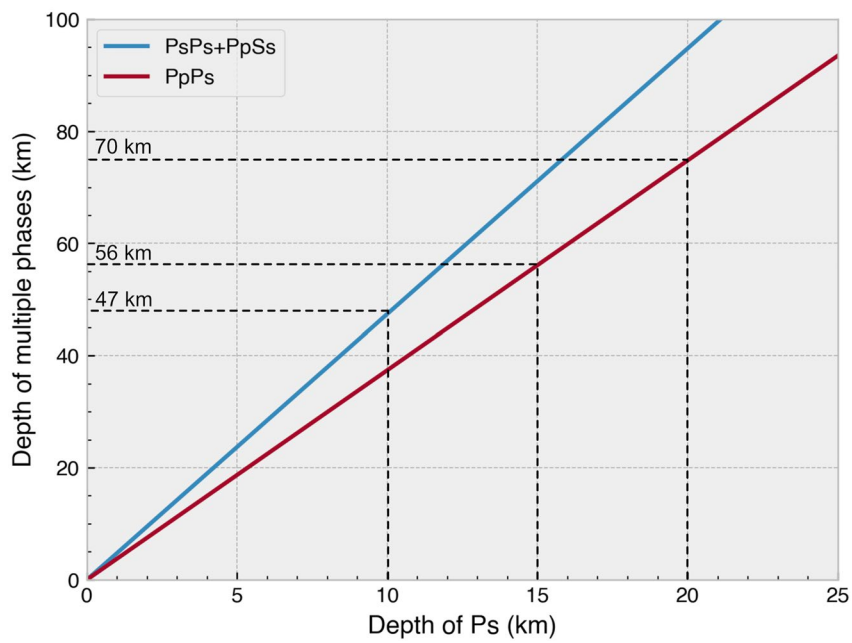

Figure 9. The depth relationship between the Ps phase and its multiple phases.

5. Cenozoic Magmatic Activity Under the ARSZ

Previous regional geophysical results have revealed crustal weak layers in the southern Dianzhong sub-block, with features such as low S-wave velocity (e.g., Bao, Sun, et al., 2015; Fu et al., 2017; Z. Zhang et al., 2020), high crustal Poisson's ratio (L. Zhang et al., 2020), high electrical conductivity (N. Yu et al., 2020), strong Lg-wave attenuation (He et al., 2021), extensive hot spring distribution (Shi & Wang, 2017) and high surface heat flow (Tao & Shen, 2008). In this study, the crustal low-velocity zone (LVZ1) is observed in the ARSZ, which may be a part of the crustal weak zones in the southern Dianzhong sub-block. However, the source of the crustal weak zones is still under debate. Crustal-scale seismic studies suggest that the crustal weak zones are parts of the lower crustal flow from central Tibet. although they may be blocked by the large igneous province in the northern part of the Dianzhong sub-block (e.g., Bao, Sun, et al., 2015; He et al., 2021). On the other hand, previous studies using data from a short-period dense array in the same study region show that the crustal averaged Poisson's ratio in the ARSZ is significantly higher than that in the surrounding areas (L. Zhang et al., 2020). The upper crustal velocity structures revealed by the short-period dense array contain a high-velocity zone under the gold deposits, indicating granitoid intrusions produced by Cenozoic magmatism (Zheng et al., 2021). These results suggest that lower crustal partial melting results from the Cenozoic magmatism beneath the RRF rather than the southeastward transportation of the lower crustal flow.

The thickness of the lithosphere in the Dianzhong sub-block and the Indochina block is less than 80 km in the global model (Pasyanos et al., 2014). Regional S-wave receiver function studies show that the LAB is at depths of ∼70–80 km in our study region (D. Yu & Wang, 2018; Hu et al., 2012). Consistent with previous observations, our CCP stacking and S-wave velocity images reveal that the LAB is at ∼70 km depth, indicating lithospheric thinning. P-wave tomography shows a high-velocity zone at ∼400 km depth under the Yangtze craton, indicating lithospheric delamination (Huang et al., 2019). Meanwhile, seismic images of the upper mantle show low-velocity zones under the Indochina block and the southern Dianzhong sub-block from ∼70 km depth to ∼300 km depth (e.g., Fu et al., 2017; Huang et al., 2019; Z. Zhang et al., 2020). Therefore, the weak crustal zones and the thinning of the lithosphere may be caused by upper mantle upwelling after lithospheric delamination.

In the Indochina block, the lithospheric thickness in the LITHOS 1.0 model is approximately 50–60 km, which is smaller than the 60–80 km thickness of the Yangtze craton (Pasyanos et al., 2014). Revealed by Pn wave and ambient noise tomography, P and S velocities in the uppermost mantle under the Indochina block are much lower than those under the Yangtze craton. These phenomena are consistent with mean features in our velocity model, but our high-resolution image shows lateral heterogeneities in the uppermost mantle between the Indochina block and ARSZ, implying that the two regions may have experienced different tectonic activities. From the Carboniferous to the Early Triassic, the closure and opening of the old Tethys Ocean formed a series of magmatic activities along the western ALSF (J.-H. Wang et al., 2001; Lai et al., 2014; Q. Wang et al., 2019). Sr–Nd–Pb isotopic characteristics suggest that the volcanic rocks in the Early Triassic originated from a MORB-like source (Fan et al., 2010; H. Liu et al., 2014), indicating asthenospheric upwelling and lithospheric thinning in this postcollisional epoch.

In contrast to the Indochina block, magmatic activity along the ARSZ mainly occurred in the early Cenozoic because the continuous orogeny along the ARSZ caused by the India-Asian collision resulted in crustal thickening in SE Tibet during this epoch (J.-H. Wang et al., 2001; Leloup et al., 1995; Searle et al., 2010; Tapponnier et al., 1990). The orogenic Au deposits and porphyry Cu-Au-Mo deposits were formed during the same period (e.g., Deng et al., 2015; J. Zhang et al., 2017; Y. Chen et al., 2014). The isotopic geochemical analysis of these magmatic and metamorphic rocks indicates that the magmatic activity originated from both the melting lower crust and the metasomatically enriched mantle (J.-H. Wang et al., 2001; J. Liu et al., 2020; L.-L. Xu, Bi, et al., 2019). The ARSZ has undergone large-scale shearing since 35 Ma (Leloup et al., 1995; Tapponnier et al., 1990). A set of high-K alkaline magmatic rock belts developed along the ARSZ from Eocene to Oligocene (Chung et al., 1997; Lu et al., 2013). Geological dating and isotopic geochemical analysis conclude that high-K alkaline magmatic rocks are associated with lithospheric delamination and upper mantle upwelling. Combining the lithospheric thinning and the crustal low-velocity zones observed in this study, we infer that since ∼35 Ma, as the stress state of the ARSZ changed (from thrust to strike-slip), the over thickened lithosphere delaminated, leading to lithospheric thinning and upwelling of the asthenosphere. The upwelling emplaced into the crust and resulted in partial melting of the mid-lower crust. Then, after ∼23 Ma, a high $^{87}Sr/^{86}Sr$ value of metamorphism implies magma along the ARSZ mainly from ancient crustal basement rocks instead of the asthenosphere (J.

Liu et al., 2020). Taking into account the high level of current geothermal activity (Shi & Wang, 2017; Tao & Shen, 2008), we infer that after asthenospheric upwelling, the lithosphere returned to a stable state characterized by relatively high velocity. However, a high level of geothermal activity (Shi & Wang, 2017) indicates that the crust is still in a hot environment, which may maintain the partial melting of the mid-lower crust.

6. Conclusions

We used the receiver function method and its derivative methods, such as the CCP stacking and the joint inversion of the PRFs and the surface wave dispersions, to image the crustal and uppermost mantle structures across the ARSZ. To evaluate the reliability of our results, we use the SEM-FK hybrid method to simulate teleseismic waveforms.

Main features such as interface topography and crustal low-velocity zones are confirmed with comparison between synthetic and observed CCP stacking images. The images reveal a flat Moho across the ARSZ. A weak zone with low velocity is obvious in the mid-lower crust just beneath the ARSZ. We also observe the LAB at ∼70 km depth and low-velocity zones under the LAB, indicating lithospheric thinning. The low-velocity zones in the uppermost mantle under the Indochina block and ARSZ also exhibit lateral heterogeneities.

Integrating the isotopic geochemical analysis and seismic images, we speculate that in the Early Triassic, lithospheric thinning under the Indochina block was formed during the postcollision period of the closure of the old Tethys Ocean. In the early Cenozoic, the Indo-Asian collision led to the thickening of the crust and lithosphere. The thickened lithosphere has been delaminated since ∼35 Ma, resulting in asthenospheric upwelling and partial melting of the mid-lower crust. The magma and the ore-forming flow may have formed during these periods and uplifted to the surface along the ARSZ.

Data Availability Statement

The waveform data around P arrival and receiver functions waveforms for this study can be downloaded at https://osf.io/97bs5/. The seismic data of ChinArray was provided by the China Seismic Array Data Management Center at the Institute of Geophysics, China Earthquake Administration (ChinArray DMC, https://doi.org/10.12001/ChinArray.Data). The Rayleigh wave dispersion data is download from CU-Boulder web site (http://ciei.colorado.edu/DispMaps/). The SWChinaCVM-1.0 community velocity model used in this study is downloaded from https://github.com/liuyingustc/SWChinaCVM. The velocity model used for correction of Ps-P time difference can be downloaded from the supplementary file of Z. Zhang et al. (2020). The receiver functions and the CCP stacking are computed using the Seispy (https://doi.org/10.5281/zenodo.3992424).

Acknowledgments
This study was supported by the National Key Research and Development Program of China (2016YFC0600302), the National Natural Science Foundations of China (42174056), the Postgraduate Research & Practice Innovation Program of Jiangsu Province, China (KYCX20_0059). We thank Prof. M. Bostock (editor), the Associate Editor, and two anonymous reviewers for their constructive advice. We thank Dr. Jiatie Pan and Prof. Xuewei Bao for providing their surface wave datasets (Bao, Song, & Li, 2015; Pan et al., 2015). We also would like to thank Prof. Mingjie Xu and Dr. Kai Wang for fruitful discussions. The joint inversion of the receiver functions and the surface wave is computed using the CPS330 (Herrmann, 2013). Figures are made by GMT 6 (Wessel et al., 2019) and Matplotlib (Hunter, 2007).

References

Bao, X., Song, X., & Li, J. (2015). High-resolution lithospheric structure beneath Mainland China from ambient noise and earthquake surface-wave tomography. *Earth and Planetary Science Letters*, *417*, 132–141. https://doi.org/10.1016/j.epsl.2015.02.024

Bao, X., Sun, X., Xu, M., Eaton, D. W. D. W., Song, X., Wang, L., et al. (2015). Two crustal low-velocity channels beneath SE Tibet revealed by joint inversion of Rayleigh wave dispersion and receiver functions. *Earth and Planetary Science Letters*, *415*, 16–24. https://doi.org/10.1016/j.epsl.2015.01.020

Brocher, T. M. (2005). Empirical relations between elastic wavespeeds and density in the Earth's crust. *Bulletin of the Seismological Society of America*, *95*(6), 2081–2092. https://doi.org/10.1785/0120050077

Chen, L., Wen, L., & Zheng, T. (2005). A wave equation migration method for receiver function imaging: 2. Application to the Japan subduction zone. *Journal of Geophysical Research*, *110*(B11). https://doi.org/10.1029/2005jb003666

Chen, X., Liu, J., Tang, Y., Song, Z., & Cao, S. (2015). Contrasting exhumation histories along a crustal-scale strike-slip fault zone: The Eocene to Miocene Ailao Shan-Red River shear zone in southeastern Tibet. *Journal of Asian Earth Sciences*, *114*, 174–187. https://doi.org/10.1016/j.jseaes.2015.05.020

Chen, Y., Yao, S., & Pan, Y. (2014). Geochemistry of lamprophyres at the Daping gold deposit, Yunnan Province, China: Constraints on the timing of gold mineralization and evidence for mantle convection in the eastern Tibetan Plateau. *Journal of Asian Earth Sciences*, *93*, 129–145. https://doi.org/10.1016/j.jseaes.2014.07.033

China Geology Survey. (2002). *Geological map of the People's Republic of China (1:2 500 000) [map]*. Sinomaps Press.

Chung, S.-L., Lee, T.-Y., Lo, C.-H., Wang, P.-L., Chen, C.-Y., Yem, N. T., et al. (1997). Intraplate extension prior to continental extrusion along the Ailao Shan–Red River shear zone. *Geology*, *25*(4), 311–314. https://doi.org/10.1130/0091-7613(1997)025<0311:IEPTCE>2.3.CO

Crotwell, H. P., Owens, T. J., & Ritsema, J. (1999). The TauP toolkit: Flexible seismic travel-time and ray-path utilities. *Seismological Research Letters*, *70*(2), 154–160. https://doi.org/10.1785/gssrl.70.2.154

Deng, J., Wang, Q., Li, G., & Zhao, Y. (2015). Structural control and Genesis of the Oligocene Zhenyuan orogenic gold deposit, SW China. *Ore Geology Reviews*, *65*, 42–54. https://doi.org/10.1016/j.oregeorev.2014.08.002

Fan, W., Wang, Y., Zhang, A., Zhang, F., & Zhang, Y. (2010). Permian arc–back-arc basin development along the Ailaoshan tectonic zone: Geochemical, isotopic and geochronological evidence from the Mojiang volcanic rocks, Southwest China. *Lithos*, *119*(3–4), 553–568. https://doi.org/10.1016/j.lithos.2010.08.010

Frederiksen, A. W., & Bostock, M. G. (2000). Modelling teleseismic waves in dipping anisotropic structures. *Geophysical Journal International*, *141*(2), 401–412. https://doi.org/10.1046/j.1365-246X.2000.00090.x

Fu, Y. V., Gao, Y., Li, A., Li, L., & Chen, A. (2017). Lithospheric structure of the southeastern margin of the Tibetan Plateau from Rayleigh wave tomography. *Journal of Geophysical Research: Solid Earth*, *122*(6), 4631–4644. https://doi.org/10.1002/2016JB013096

He, X., Zhao, L., Xie, X., Tian, X., & Yao, Z. (2021). Weak crust in Southeast Tibetan plateau revealed by Lg-wave attenuation tomography: Implications for crustal material escape. *Journal of Geophysical Research: Solid Earth*, *126*(3). https://doi.org/10.1029/2020JB020748

Herrmann, R. B. (2013). Computer programs in seismology: An evolving tool for instruction and research. *Seismological Research Letters*, *84*(6), 1081–1088. https://doi.org/10.1785/0220110096

Hu, J., Yang, H., Xu, X., Wen, L., & Li, G. (2012). Lithospheric structure and crust–mantle decoupling in the southeast edge of the Tibetan Plateau. *Gondwana Research*, *22*(3–4), 1060–1067. https://doi.org/10.1016/j.gr.2012.01.003

Huang, Z., Wang, L., Xu, M., Zhao, D., Mi, N., & Yu, D. (2019). P and S wave tomography beneath the SE Tibetan plateau: Evidence for lithospheric delamination. *Journal of Geophysical Research: Solid Earth*, *124*(10), 10292–10308. https://doi.org/10.1029/2019JB017430

Huang, Z., Wang, P., Xu, M., Wang, L., Ding, Z., Wu, Y., et al. (2015). Mantle structure and dynamics beneath SE Tibet revealed by new seismic images. *Earth and Planetary Science Letters*, *411*, 100–111. https://doi.org/10.1016/j.epsl.2014.11.040

Hunter, J. D. (2007). Matplotlib: A 2D graphics environment. *Computing in Science & Engineering*, *9*(3), 90–95. https://doi.org/10.1109/MCSE.2007.55

Julià, J., Ammon, C. J., Herrmann, R. B., & Correig, A. M. (2000). Joint inversion of receiver function and surface wave dispersion observations. *Geophysical Journal International*, *143*(1), 99–112. https://doi.org/10.1046/j.1365-246x.2000.00217.x

Kennett, B. L. N., Engdahl, E. R., & Buland, R. (1995). Constraints on seismic velocities in the Earth from traveltimes. *Geophysical Journal International*, *122*(1), 108–124. https://doi.org/10.1111/j.1365-246X.1995.tb03540.x

Lai, C.-K., Meffre, S., Crawford, A. J., Zaw, K., Xue, C.-D., & Halpin, J. A. (2014). The Western Ailaoshan volcanic belts and their SE Asia connection: A new tectonic model for the eastern Indochina block. *Gondwana Research*, *26*(1), 52–74. https://doi.org/10.1016/j.gr.2013.03.003

Leloup, P. H., Lacassin, R., Tapponnier, P., Schärer, U., Zhong, D., Liu, X., et al. (1995). The Ailao Shan-Red River shear zone (Yunnan, China), tertiary transform boundary of Indochina. *Tectonophysics*, *251*(1), 3–84. https://doi.org/10.1016/0040-1951(95)00070-4

Li, J., Song, X., Zhu, L., & Deng, Y. (2017). Joint inversion of surface wave dispersions and receiver functions with P velocity constraints: Application to southeastern Tibet. *Journal of Geophysical Research: Solid Earth*, *122*(9), 7291–7310. https://doi.org/10.1002/2017JB014135

Ligorría, J. P., & Ammon, C. J. (1999). Iterative deconvolution and receiver-function estimation. *Bulletin of the Seismological Society of America*, *89*(5), 1395–1400. https://doi.org/10.1785/BSSA0890051395

Liu, H., Wang, Y., Fan, W., Zi, J., Cai, Y., & Yang, G. (2014). Petrogenesis and tectonic implications of Late-Triassic high ε Nd(t)-ε Hf(t) granites in the Ailaoshan tectonic zone (SW China). *Science China Earth Sciences*, *57*(9), 2181–2194. https://doi.org/10.1007/s11430-014-4854-z

Liu, J., Chen, X., Tang, Y., Song, Z., & Wang, W. (2020). The Ailao Shan–Red River shear zone revisited: Timing and tectonic implications. *GSA Bulletin*, *132*(5–6), 1165–1182. https://doi.org/10.1130/B35220.1

Liu, Y., Yao, H., Zhang, H., & Fang, H. (2021). The community velocity model V.1.0 of Southwest China, constructed from joint body- and surface-wave travel-time tomography. *Seismological Research Letters*, *92*(5), 2972–2987. https://doi.org/10.1785/0220200318

Lü, Y., Zhang, Z., Pei, S., Sandvol, E., Xu, T., & Liang, X. (2014). 2.5-Dimensional tomography of uppermost mantle beneath Sichuan–Yunnan and surrounding regions. *Tectonophysics*, *627*, 193–204. https://doi.org/10.1016/j.tecto.2013.03.008

Lu, Y.-J., Kerrich, R., Mccuaig, T. C., Li, Z.-X., Hart, C. J. R., Cawood, P. A., et al. (2013). Geochemical, Sr-Nd-Pb, and Zircon Hf-O isotopic compositions of eocene-oligocene shoshonitic and potassic adakite-like felsic intrusions in western Yunnan, SW China: Petrogenesis and tectonic implications. *Journal of Petrology*, *54*(7), 1309–1348. https://doi.org/10.1093/petrology/egt013

Metcalfe, I. (1996). Pre-Cretaceous evolution of SE Asian terranes. *Geological Society, London, Special Publications*, *106*(1), 97–122. https://doi.org/10.1144/GSL.SP.1996.106.01.09

Metcalfe, I. (2002). Permian tectonic framework and palaeogeography of SE Asia. *Journal of Asian Earth Sciences*, *20*(6), 551–566. https://doi.org/10.1016/S1367-9120(02)00022-6

Pan, J.-T., Li, Y.-H., Wu, Q.-J., & Ding, Z.-F. (2015). Phase velocity maps of Rayleigh waves in the southeast Tibetan Plateau (in Chinese with English abstract). *Chinese Journal of Geophysics*, *58*(11), 3993–4006. https://doi.org/10.6038/cjg20151109

Pasyanos, M. E., Masters, T. G., Laske, G., & Ma, Z. (2014). LITHO1.0: An updated crust and lithospheric model of the Earth. *Journal of Geophysical Research: Solid Earth*, *119*(3), 2153–2173. https://doi.org/10.1002/2013JB010626

Schoenbohm, L. M., Burchfiel, B. C., Liangzhong, C., & Jiyun, Y. (2006). Miocene to present activity along the Red River fault, China, in the context of continental extrusion, upper-crustal rotation, and lower-crustal flow. *The Geological Society of America Bulletin*, *118*(5–6), 672–688. https://doi.org/10.1130/B25816.1

Searle, M. P., Yeh, M.-W., Lin, T.-H., & Chung, S.-L. (2010). Structural constraints on the timing of left-lateral shear along the Red River shear zone in the Ailao Shan and Diancang Shan Ranges, Yunnan, SW China. *Geosphere*, *6*(4), 316–338. https://doi.org/10.1130/GES00580.1

Shen, W., Ritzwoller, M. H., Kang, D., Kim, Y. H., Lin, F. C., Ning, J., et al. (2016). A seismic reference model for the crust and uppermost mantle beneath China from surface wave dispersion. *Geophysical Journal International*, *206*(2), 954–979. https://doi.org/10.1093/gji/ggw175

Shi, Z., & Wang, G. (2017). Evaluation of the permeability properties of the Xiaojiang Fault Zone using hot springs and water wells. *Geophysical Journal International*, *209*(3), 1526–1533. https://doi.org/10.1093/gji/ggx113

Sun, X., Zhang, Y., Xiong, D., Sun, W., Shi, G., Zhai, W., & Wang, S. (2009). Crust and mantle contributions to gold-forming process at the Daping deposit, Ailaoshan gold belt, Yunnan, China. *Ore Geology Reviews*, *36*(1–3), 235–249. https://doi.org/10.1016/j.oregeorev.2009.05.002

Tao, W., & Shen, Z. (2008). Heat flow distribution in Chinese continent and its adjacent areas. *Progress in Natural Science*, *18*(7), 843–849. https://doi.org/10.1016/j.pnsc.2008.01.018

Tapponnier, P., Lacassin, R., Leloup, P. H., Schärer, U., Dalai, Z., Haiwei, W., et al. (1990). The Ailao Shan/Red River metamorphic belt: Tertiary left-lateral shear between Indochina and South China. *Nature*, *343*(6257), 431–437. https://doi.org/10.1038/343431a0

Tapponnier, P., Zhiqin, X., Roger, F., Meyer, B., Arnaud, N., Wittlinger, G., & Jingsui, Y. (2001). Oblique stepwise rise and growth of the Tibet Plateau. *Science*, *294*(5547), 1671–1677. https://doi.org/10.1126/science.105978

Tong, P., Chen, C., Komatitsch, D., Basini, P., & Liu, Q. (2014). High-resolution seismic array imaging based on an SEM-FK hybrid method. *Geophysical Journal International*, *197*(1), 369–395. https://doi.org/10.1093/gji/ggt508

Tong, P., Komatitsch, D., Tseng, T.-L., Hung, S.-H., Chen, C.-W., Basini, P., & Liu, Q. (2014). A 3-D spectral-element and frequency-wave number hybrid method for high-resolution seismic array imaging. *Geophysical Research Letters*, *41*(20), 7025–7034. https://doi.org/10.1002/2014GL061644

Wang, J.-H., Yin, A., Harrison, T. M., Grove, M., Zhang, Y.-Q., & Xie, G.-H. (2001). A tectonic model for Cenozoic igneous activities in the eastern Indo–Asian collision zone. *Earth and Planetary Science Letters*, *188*(1), 123–133. https://doi.org/10.1016/S0012-821X(01)00315-6

Wang, Q., Groves, D. I., Deng, J., Li, H., Yang, L., & Dong, C. (2019). Evolution of the Miocene Ailaoshan orogenic gold deposits, southeastern Tibet, during a complex tectonic history of lithosphere-crust interaction. *Mineralium Deposita*, *55*(6), 1085–1104. https://doi.org/10.1007/s00126-019-00922-3

Wang, X., Metcalfe, I., Jian, P., He, L., & Wang, C. (2000). The Jinshajiang–Ailaoshan suture zone, China: Tectonostratigraphy, age and evolution. *Journal of Asian Earth Sciences*, *18*(6), 675–690. https://doi.org/10.1016/S1367-9120(00)00039-0

Wessel, P., Luis, J. F., Uieda, L., Scharroo, R., Wobbe, F., Smith, W. H. F., & Tian, D. (2019). The generic mapping tools version 6. *Geochemistry, Geophysics, Geosystems*, *20*(11), 5556–5564. https://doi.org/10.1029/2019GC008515

Xu, L.-L., Bi, X.-W., Hu, R.-Z., Tang, Y.-Y., Wang, X.-S., Huang, M.-L., et al. (2019). Contrasting whole-rock and mineral compositions of ore-bearing (Tongchang) and ore-barren (Shilicun) granitic plutons in SW China: Implications for petrogenesis and ore Genesis. *Lithos*, *336–337*, 54–66. https://doi.org/10.1016/j.lithos.2019.03.031

Xu, M., Huang, Z., Wang, L., Xu, M., Zhang, Y., Mi, N., et al. (2020). Sharp lateral Moho variations across the SE Tibetan margin and their implications for Plateau growth. *Journal of Geophysical Research: Solid Earth*, *125*(5), e2019JB018117. https://doi.org/10.1029/2019JB018117

Xu, Q., Pei, S., Yuan, X., Zhao, J., Liu, H., Tu, H., & Chen, S. (2019). Seismic evidence for lateral asthenospheric flow beneath the northeastern Tibetan plateau derived from *S* receiver functions. *Geochemistry, Geophysics, Geosystems*, *20*(2), 883–894. https://doi.org/10.1029/2018GC007986

Yang, H., Peng, H., & Hu, J. (2017). The lithospheric structure beneath southeast Tibet revealed by P and S receiver functions. *Journal of Asian Earth Sciences*, *138*, 62–71. https://doi.org/10.1016/j.jseaes.2017.02.001

Yu, D., & Wang, P. (2018). The lithospheric structures beneath the Au deposits in the south Ailaoshan shear zone from receiver functions: Implications for lithospheric thinning and the magma channel (in Chinese with English abstract). *Geological Journal of China Universities*, *24*(4), 516–524.

Yu, N., Unsworth, M., Wang, X., Li, D., Wang, E., Li, R., et al. (2020). New Insights into crustal and mantle flow beneath the Red River fault zone and adjacent areas on the southern margin of the Tibetan Plateau revealed by a 3-D Magnetotelluric study. *Journal of Geophysical Research: Solid Earth*, *125*(10), e2020JB019396. https://doi.org/10.1029/2020JB019396

Zhang, J., Deng, J., Chen, H., Yang, L., Cooke, D., Danyushevsky, L., & Gong, Q. (2014). LA-ICP-MS trace element analysis of pyrite from the Chang'an gold deposit, Sanjiang region, China: Implication for ore-forming process. *Gondwana Research*, *26*(2), 557–575. https://doi.org/10.1016/j.gr.2013.11.003

Zhang, J., Wang, H., Li, S., & Li, T. (2017). Paleogene magmatism and gold metallogeny of the Jinping terrane in the Ailaoshan ore belt, Sanjiang Tethyan Orogen (SW China): Geology, deposit type and tectonic setting. *Ore Geology Reviews*, *91*, 620–637. https://doi.org/10.1016/j.oregeorev.2017.08.032

Zhang, L., Bai, Z., Xu, T., Wu, Z., Huang, M., Yu, G., et al. (2020). Cenozoic magmatic activity and oblique uplifting of the Ailao Mountain: Evidence from a short-period dense seismic array. *Science China Earth Sciences*, *63*(9), 1294–1308. https://doi.org/10.1007/s11430-019-9616-y

Zhang, Z., Yao, H., & Yang, Y. (2020). Shear wave velocity structure of the crust and upper mantle in Southeastern Tibet and its geodynamic implications. *Science China Earth Sciences*, *63*(9), 1278–1293. https://doi.org/10.1007/s11430-020-9625-3

Zhao, J., Yuan, X., Liu, H., Kumar, P., Pei, S., Kind, R., et al. (2010). The boundary between the Indian and Asian tectonic plates below Tibet. *Proceedings of the National Academy of Sciences of the United States of America*, *107*(25), 11229–11233. https://doi.org/10.1073/pnas.1001921107

Zhao, L., Paul, A., Guillot, S., Solarino, S., Malusà, M. G., Zheng, T., et al. (2015). First seismic evidence for continental subduction beneath the Western Alps. *Geology*, *43*(9), 815–818. https://doi.org/10.1130/G36833.1

Zheng, M., Bai, Z., Xu, T., & Badal, J. (2021). Upper crustal velocity structure of the Ailaoshan-Red River shear zone and its implication for Cenozoic tectonic-magmatic activity: Evidence from ambient noise tomography using short-period dense seismic array. *Physics of the Earth and Planetary Interiors*, *311*, 106643. https://doi.org/10.1016/j.pepi.2021.106643